



Article

Hybrid Nanofluid Flow Induced by an Oscillating Disk Considering Surface Catalyzed Reaction and Nanoparticles Shape Factor

Muhammad Ramzan ^{1,*}, Saima Riasat ¹, Saleh Fahad Aljurbua ², Hassan Ali S. Ghazwani ³ and Omar Mahmoud ⁴

¹ Department of Computer Science, Bahria University, Islamabad 44000, Pakistan; saimaqau@live.com

² Department of Mathematics, College of Science, Qassim University, Buriadah 51452, Saudi Arabia; s.aljurbua@qu.edu.sa

³ Department of Mechanical Engineering, Faculty of Engineering, Jazan University, Jazan 45124, Saudi Arabia; hghazwani@jazanu.edu.sa

⁴ Faculty of Engineering & Technology, Future University in Egypt, New Cairo 11835, Egypt; omar.saad@fue.edu.eg

* Correspondence: mramzan@bahria.edu.pk

Abstract: Lately, a new class of nanofluids, namely hybrid nanofluids, has been introduced that performs much better compared with the nanofluids when a healthier heat transfer rate is the objective of the study. Heading in the same direction, the present investigation accentuates the unsteady hybrid nanofluid flow involving CuO , $Al_2O_3/C_2H_6O_2$ achieved by an oscillating disk immersed in the porous media. In a study of the homogeneous and heterogeneous reactions, the surface catalyzed reaction was also considered to minimize the reaction time. The shape factors of the nanoparticles were also taken into account, as these play a vital role in assessing the thermal conductivity and heat transfer rate of the system. The assumed model is presented mathematically in the form of partial differential equations. The system is transformed by invoking special similarity transformations. The Keller Box scheme was used to obtain numerical and graphical results. It is inferred that the blade-shaped nanoparticles have the best thermal conductivity that boosts the heat transfer efficiency. The oscillation and surface-catalyzed chemical reactions have opposite impacts on the concentration profile. This analysis also includes a comparison of the proposed model with a published result in a limiting case to check the authenticity of the presented model.

Keywords: heat transfer analysis; hybrid nanofluid; modeling and simulation; numerical solution



Citation: Ramzan, M.; Riasat, S.; Aljurbua, S.F.; Ghazwani, H.A.S.; Mahmoud, O. Hybrid Nanofluid Flow Induced by an Oscillating Disk Considering Surface Catalyzed Reaction and Nanoparticles Shape Factor. *Nanomaterials* **2022**, *12*, 1794. <https://doi.org/10.3390/nano12111794>

Academic Editor: Lou Kondic

Received: 16 April 2022

Accepted: 21 May 2022

Published: 24 May 2022

Publisher's Note: MDPI stays neutral with regard to jurisdictional claims in published maps and institutional affiliations.



Copyright: © 2022 by the authors. Licensee MDPI, Basel, Switzerland. This article is an open access article distributed under the terms and conditions of the Creative Commons Attribution (CC BY) license (<https://creativecommons.org/licenses/by/4.0/>).

1. Introduction

The importance of base fluids (orthodox liquids) for thermal transfer in industrial processes cannot be denied. Generally, these liquids possess poor heat transferability. To overcome this barrier, nano-sized (<100 nm) particles are added to improve the thermal transport capability. This idea was initially pitched by Choi and Eastman [1]. Generally, it is an accepted truth that solid particles have higher thermal heat conduction when compared with liquids. Thus, the inclusion of nano-sized particles in customary fluids improved their thermal conduction comprehensively. These solid particles are identified as nanoparticles. The amalgamation of the base fluid and the nanoparticles is termed a nanofluid. Eastman [2], in an experimental work, claimed that the addition of a small amount of nano-sized solid material particles can improve the thermal conduction of conventional liquids. The conclusion of this study revealed that the thermal performance of ethylene glycol (the base fluid) was improved by 40–50% after the addition of copper nanoparticles or carbon nanotubes (CNTs) at <1% (volume fraction). This is because nanofluids have a pivoting role in electro-mechanical gadgets, heat exchange, advanced

cooling systems, etc. A good number of experimental and theoretical studies have been conducted with various combinations of the nanoparticles and base fluids [3–12].

Lately, an advanced form of nanofluids has been introduced, namely hybrid nanofluids. The hybrid nanofluids comprise an orthodox liquid and two or more kinds of nanoparticles. Hybrid nanofluids are more efficient than customary nanofluids as far as heat transport is concerned. The synthesis of a hybrid nanofluid comprising Al_2O_3 -Cu/water using a two-step method was conducted experimentally by Suresh et al. [13]. The study revealed an enhancement of 12.11% in thermal conduction for a 2% volume fraction. Madhesh et al. [14] experimentally discussed a copper–titania hybrid nanofluid and copper–titania hybrid nanocomposite flows with volume concentrations of 0.1–2.0%. The results divulged that the rate of heat flux is improved by 49% for a volume fraction of up to 1%. An experiment was conducted by Toghraie et al. [15] on the synthesis of a ZnO–TiO₂/EG hybrid nanofluid to demonstrate the impacts of the nanoparticles' concentration and temperature on the hybrid nanofluid's conduction. The outcome was interesting, revealing that the thermal conduction was 32% for a volume fraction of 3.5% at 50 °C. Parallel to these experimental works, researchers have also focused on theoretical studies focusing on hybrid nanofluid flows. Gul et al. [16] conducted a comparative study of Hamilton–Crosser, and Yamada–Ota hybrid nanofluid models containing titanium oxide and silicon carbide nanoparticles added into diathermic oil. The hybrid nanofluid was taken through stimulation with a magnetic dipole and the flow was assumed over an extended surface. The salient outcome revealed that the Yamada–Ota model was far better in terms of heat transfer performance than the Hamilton–Crosser hybrid nanofluid flow model. Water-based ternary hybrid nanofluid flows with numerous nanoparticle shapes including spheres, cylinders, and platelets of aluminum oxide, carbon nanotubes, and graphene, respectively, between two parallel sheets, were examined theoretically by Arif et al. [17]. An enhancement in thermal heat transfer of 33.67% was observed for the ternary hybrid nanofluid flow when compared with the unitary nanofluid flow. Recent studies featuring hybrid nanofluid flow in various scenarios may be observed in [18–22].

The problems related to fluid flow over rotating disks are among the well-known active research topics owing to their applicability in many engineering applications encompassing hard disks, jet motors, turbine systems, etc. This is why the subject of rotating flow has gained massive attention and has been welcomed by researchers [23–28].

Studies associated with chemical reactions attract the interest of researchers due to their importance in various physical and chemical processes. The molecular diffusion of species in such processes, whether inside or on the surface, cannot be overlooked. Many chemical, biological, and physical processes involve chemical reactions. Therefore, to study these reacting systems, the study of homogeneous and heterogeneous reactions is essential. The presence of a catalyst is essential for a reaction to proceed at a better speed. A reaction occurring on the surface of absorbent media is also a type of heterogeneous reaction and is known as a surface-catalyzed chemical reaction [29]. Elattar et al. [30] computed the hybrid nanofluid flow with Hall current over a slender surface. Recent work focused on chemical reactions may be found in [31–33].

The published literature and referenced publications demonstrate a plethora of investigations focusing on nanofluid flows. Nonetheless, there are only a few studies that have shown a comparison of hybrid flows over a variety of geometries. The current study is innovative in several ways: Firstly, the flow over a fluctuating rotating disk was combined with homogeneous–heterogeneous reactions and surface-catalyzed chemical reaction. Secondly, the heat transfer rate was studied, considering the numerous shapes. Thirdly, porous media were incorporated for surface catalysis. To solve the problem, various numerical techniques have been used by various researchers [34–38]. The numerical results were tabulated by using the Keller Box scheme, and the velocity, temperature, and concentration profiles were sketched graphically. Finally, the numerical solution included a validation table to ensure the validity of the proposed model. This research intended to provide answers to the following essential questions:

- Which is the best nanoparticle shape to manufacture a hybrid nanofluid?
- Does a fluctuating rotating disk influence the reaction rate?
- Do the Wall temperature and disk fluctuation both affect the heat transfer rate?
- Is there a significant impact of the surface catalyzed reaction on the rate of reaction?
- Is the axial velocity profile affected by variations in the volume fraction?

2. Mathematical Model

Consider an oscillating disk with a velocity $\dot{a}(t)$ immersed in porous media with CuO , $Al_2O_3/C_2H_6O_2$, a hybrid nanofluid with temperature-dependent thermal conductivity. The angular velocity of the disk is $\Omega(t)$. The velocity components in the radial, azimuthal, and axial directions are u, v and w . Homogeneous and heterogeneous reactions also occur on the surface of the absorbent media and the disk. The flow diagram is given in Figure 1.

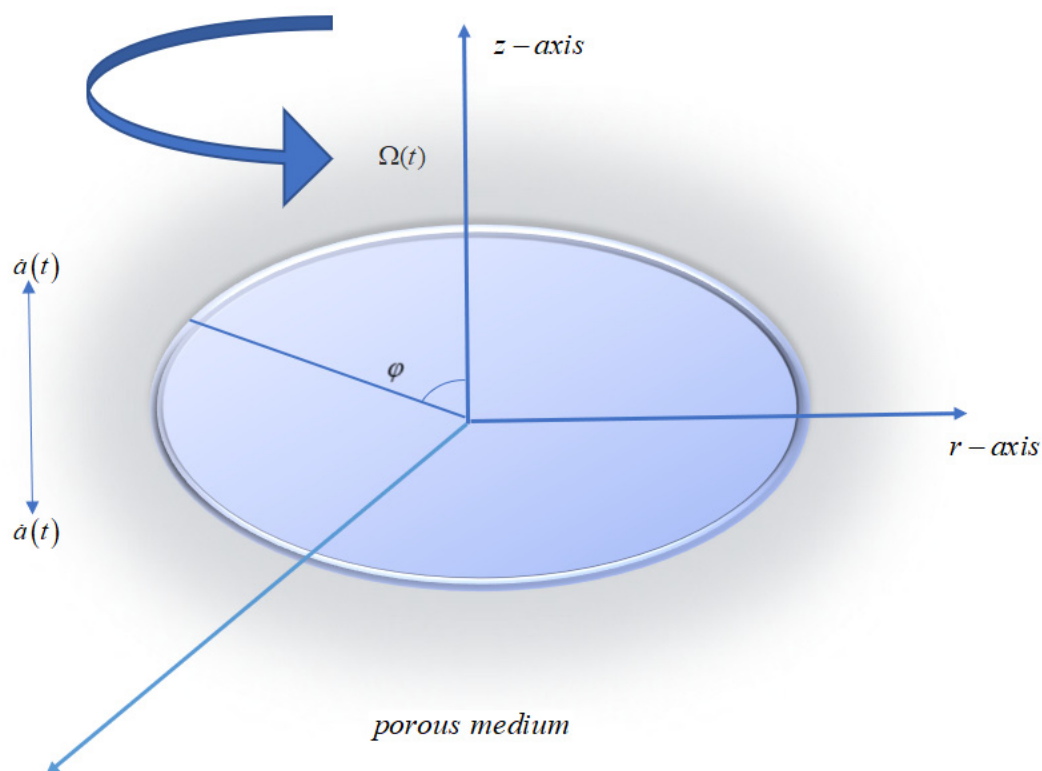


Figure 1. Flow geometry.

The geometrical and mathematical models drawn under the above assumption are as follows:

The temperature is time-dependent and can be taken in the form [26]:

$$\Delta T = T_w(t) - T_\infty, \quad (1)$$

where T_∞ is the ambient fluid temperature and $T_w(t)$ is as follows [26]:

$$T_w(t) = T_\infty + ca(t)^{-2\alpha}, \quad (2)$$

The following equation represents the reaction phenomenon [33]:



Under the above assumption, the mathematical model is as described by [33]:

$$\frac{u}{r} + \frac{\partial u}{\partial r} + \frac{\partial w}{\partial z} = 0, \tag{5}$$

$$\frac{\partial u}{\partial t} + u \frac{\partial u}{\partial r} + w \frac{\partial u}{\partial z} - \frac{v^2}{r} = \frac{1}{\rho_{hnf}} \frac{\partial p}{\partial r} + \frac{\mu_{hnf}}{\rho_{hnf}} \left[\frac{\partial^2 u}{\partial r^2} + \frac{1}{r} \frac{\partial u}{\partial r} + \frac{\partial^2 u}{\partial z^2} - \frac{u}{r^2} \right] - \frac{\mu_{hnf}}{\rho_{hnf}} \frac{u}{k^*}, \tag{6}$$

$$\frac{\partial v}{\partial t} + u \frac{\partial v}{\partial r} + w \frac{\partial v}{\partial z} + \frac{vu}{r} = \frac{\mu_{hnf}}{\rho_{hnf}} \left[\frac{\partial^2 v}{\partial r^2} + \frac{1}{r} \frac{\partial v}{\partial r} + \frac{\partial^2 v}{\partial z^2} - \frac{v}{r^2} \right] - \frac{\mu_{hnf}}{\rho_{hnf}} \frac{v}{k^*}, \tag{7}$$

$$\frac{\partial w}{\partial t} + u \frac{\partial w}{\partial r} + w \frac{\partial w}{\partial z} = -\frac{1}{\rho_{hnf}} \frac{\partial p}{\partial z} + \frac{\mu_{hnf}}{\rho_{hnf}} \left[\frac{\partial^2 w}{\partial r^2} + \frac{1}{r} \frac{\partial w}{\partial r} + \frac{\partial^2 w}{\partial z^2} \right] - \frac{\mu_{hnf}}{\rho_{hnf}} \frac{w}{k^*}, \tag{8}$$

$$(\rho C_p)_{hnf} \left(\frac{\partial T}{\partial t} + u \frac{\partial T}{\partial r} + w \frac{\partial T}{\partial z} \right) = \kappa_{hnf} \left[\frac{\partial^2 T}{\partial r^2} + \frac{1}{r} \frac{\partial T}{\partial r} + \frac{\partial}{\partial z} \left(\frac{\partial T}{\partial z} \right) \right], \tag{9}$$

$$\frac{\partial C_a}{\partial t} + u \frac{\partial C_a}{\partial r} + w \frac{\partial C_a}{\partial z} = D_{A^*} \frac{\partial}{\partial z} \left(\frac{\partial C_a}{\partial z} \right) - k_c C_a C_b^2 - \tilde{S} k_s C_a, \tag{10}$$

$$\frac{\partial C_b}{\partial t} + u \frac{\partial C_b}{\partial r} + w \frac{\partial C_b}{\partial z} = D_{B^*} \frac{\partial}{\partial z} \left(\frac{\partial C_b}{\partial z} \right) + k_c C_a C_b^2 + \tilde{S} k_s C_a, \tag{11}$$

The mathematical model is subjected to constraints on the boundaries as follows:

$$u = 0, v = r\Omega(t), w = 0, T = T_w(t), D_{A^*} \frac{\partial C_a}{\partial z} = k_s C_a, D_{B^*} \frac{\partial C_b}{\partial z} = -k_s C_a \text{ at } z = 0, \tag{12}$$

$$u \rightarrow 0, v \rightarrow 0, T \rightarrow T_\infty, C_a \rightarrow C_\infty, C_b \rightarrow 0, \text{ at } z \rightarrow \infty,$$

We can then apply the following transformation [26]:

$$u = \frac{rv}{a^2(t)} f(\eta), v = \frac{rv}{a^2(t)} g(\eta), w = \frac{v}{a(t)} H(\eta), p = \frac{\rho v^2}{a^2(t)} P(\eta), C_a = C_\infty \phi, \tag{13}$$

$$C_b = C_\infty \xi, \theta(\eta) = \frac{T - T_\infty}{T_w - T_\infty}, \eta = \frac{z}{a(t)} - 1, \eta_z = \frac{1}{a(t)}, \eta_t = -\frac{\dot{a}(t)}{a(t)} (\eta + 1).$$

The thermophysical features of the nanoparticles and the base fluid are tabulated in Table 1, and Table 2 presents the sphericity values for numerous nanoparticle shapes.

Table 1. Thermophysical characteristics of C₂H₆O₂, Al₂O₃, and CuO [2,36].

Properties	CuO	C ₂ H ₆ O ₂	Al ₂ O ₃
$k \left(\frac{W}{mK} \right)$	18	0.249	40
$\rho \left(\frac{kg}{m^3} \right)$	6500	1116.6	3970
$C_p \left(JK^{-1}kg^{-1} \right)$	540	2382	765

Table 2. Sphericity values for various shapes of the nanoparticles [17,19,36].

Sphericity	Blade	Platelet	Cylinder	Brick	Sphere
ψ	0.36	0.52	0.62	0.81	1.0
Shape					

The thermophysical features in terms of the nanoparticle volume fraction for the hybrid nanofluid are as follows [36]:

$$A = \frac{\mu_{hnf}(T)}{\mu_f} = (1 - \phi_1)^{-2.5}(1 - \phi_2)^{-2.5}, \tag{14}$$

$$B = \frac{\rho_{hnf}}{\rho_f} = (1 - \phi_2) \left\{ (1 - \phi_1) + \phi_1 \frac{\rho_{s_2}}{\rho_f} \right\} + \phi_2 \frac{\rho_{s_1}}{\rho_f}, \tag{15}$$

$$C_1 = \frac{k_{hnf}}{k_{bf}} = \frac{k_{s_2} - k_{bf}(1-n) + (1-n)\phi_2(k_{bf} - k_{s_2})}{k_{s_2} - (1-n)k_{bf} + \phi_2(k_{bf} - k_{s_2})}, \tag{16}$$

$$D = \frac{k_{bf}}{k_f} = \frac{k_{s_1} - (1-n)k_f + (1-n)\phi_1(k_f - k_{s_1})}{k_{s_1} - (1-n)k_f - \phi_1(k_f - k_{s_1})}, n = \frac{3}{\psi},$$

$$E = \frac{(\rho C_p)_{hnf}}{(\rho C_p)_f} = (1 - \phi_2) \left\{ (1 - \phi_1) + \phi_1 \frac{(\rho C_p)_{s_1}}{(\rho C_p)_f} \right\} + \frac{(\rho C_p)_{s_2}}{(\rho C_p)_f} \phi_2. \tag{17}$$

The transformed mathematical model is:

$$2f' + H = 0, \tag{18}$$

$$f'' = \left(Hf' + f^2 - g^2 - S \left[\frac{\eta + 1}{2} f' + f \right] + \lambda f \right), \tag{19}$$

$$g'' = \left(Hg' + 2fg - S \left[\frac{\eta + 1}{2} g' + g \right] + \lambda g \right) \tag{20}$$

$$\frac{\partial P}{\partial z} = \left(HH' - S \left[\frac{\eta + 1}{2} H' + H \right] + \lambda H \right), \tag{21}$$

$$- \frac{PrS}{C_1 D} \left[\alpha \theta + \frac{(\eta + 1)}{2} \theta' \right] + \frac{A}{BC_1 D} PrH\theta' = (1 + \epsilon \theta) \theta'' + \epsilon \theta'^2 \tag{22}$$

$$S(\eta + 1)\phi' - h\phi' = -\frac{1}{Sc} \phi'' + K_c \phi(1 - \phi)^2 - K_{vs} \phi, \tag{23}$$

$$- S(\eta + 1)\xi' + h\xi' = \frac{\delta}{Sc} \xi'' + K_c \phi \xi^2 + K_{vs} \xi, \tag{24}$$

The transformed bounded constraints are:

$$f(0) = 0, g(0) = \omega, H(0) = 0, \theta(0) = 1, \xi'(0) = K_s \xi(0), \phi'(0) = K_s \phi(0), \tag{25}$$

$$f(\infty) \rightarrow 0, g(\infty) \rightarrow 0, \theta(\infty) \rightarrow 0, \phi(\infty) \rightarrow 1, \xi(\infty) \rightarrow 0,$$

where $a(t) = d\sqrt{1 + \frac{v_{hnf} S}{d^2} t}$ is the displacement of the oscillatory disk. The rotation parameter is $\omega = \frac{\Omega(t)a^2(t)}{v_{hnf}}$, and $S = 2\frac{a(t)\dot{a}(t)}{v_{hnf}}$ is the parameter for controlling the contraction and expansion of the disk.

Assuming both species have comparatively the same size, we have:

$$\delta = 1, \xi(\eta) + \phi(\eta) = 1, \tag{26}$$

Equations (23) and (24) will be reduced to:

$$Sc \left[K_c \phi(1 - \phi)^2 - S(\eta + 1)\phi' + h\phi' \right] = \phi'', \tag{27}$$

with the associated boundary condition:

$$\phi'(0) = K_s \phi(0), \phi(1) \rightarrow 1, \tag{28}$$

where:

$$\begin{aligned} \frac{a^2(t)}{k^*} &= \lambda, Sc = \frac{\nu_f}{D_{A^*}}, K_c = \frac{k_c C_a^2}{\Omega}, K_{vs} = S_v K_s, K_s = \frac{k_s \sqrt{\nu_f}}{D_{A^*} \sqrt{\Omega}}, \\ \delta &= \frac{D_B}{D_A}, Pr = \frac{C_p \mu_f}{k_f} S_v = \frac{\tilde{S} D_A}{\sqrt{\nu_f \Omega}}. \end{aligned} \quad (29)$$

where $\lambda, Sc, K_c, K_{vs}, K_s, \delta, Pr, S_v$ represent the porosity parameter, Schmidt number, homogeneous reaction parameter, surface catalyzed parameter, heterogeneous reaction parameter, the ratio of diffusion coefficient, Prandtl number, and parameter of interfacial area, respectively. Detailed work for the conversion of a system of partial differential equations to a system of ordinary differential equations is given in the Appendix A.

3. Numerical Scheme (Keller Box)

The transformed mathematical model is tackled by using the Keller Box scheme. The numerical procedure involves the following steps.

First, we utilize the following transformation to convert the problem into the first order.

$$f' = -\frac{H}{2}, g' = X, \theta' = Y, \phi' = Z \quad (30)$$

The transformed mathematical model is as follows:

$$H' = 2 \left(\frac{H^2}{2} - f^2 + g^2 - S \left[\frac{\eta + 1}{4} H - f \right] - \lambda f \right), \quad (31)$$

$$X' = \left(HX + 2fg - S \left[\frac{\eta + 1}{2} X + g \right] + \lambda g \right), \quad (32)$$

$$- \frac{PrS}{C_1 D} \left[\alpha \theta + \frac{(\eta + 1)}{2} Y \right] + \frac{A}{BC_1 D} PrHY = (1 + \varepsilon \theta) \theta Y' + \varepsilon Y^2 \quad (33)$$

$$Sc \left[K_c \phi (1 - \phi)^2 - S(\eta + 1)Z + HZ \right] = Z', \quad (34)$$

The boundary conditions are:

$$\begin{aligned} f(0) &= 0, g(0) = \omega, H(0) = 0, \theta(0) = 1, \phi'(0) = K_s \phi(0), \\ f(\infty) &\rightarrow 0, g(\infty) \rightarrow 0, \theta(\infty) \rightarrow 0, \phi(\infty) \rightarrow 1, \end{aligned} \quad (35)$$

Next, consider the discretization of η the axis with a step size h_j such that:

$$\eta_0 = 0, \eta_j = h_j + \eta_{j-1}, j = 1, 2, 3, \dots, J. \text{ For } J \rightarrow \infty, \eta_J = \eta_\infty. \quad (36)$$

For the point $\eta_{j-1/2}$ on the η axis, we have a central difference approximation defined by:

$$\begin{aligned} f_{j-1/2} &= \frac{f_j^i + f_{j-1}^i}{2} \\ f'_{j-1/2} &= \frac{f_j^i - f_{j-1}^i}{h_j} \end{aligned} \quad (37)$$

The discretization in the $\eta - z$ plane is explained in Figure 2.

$$z^0 = 0, z^i = z^{i-1} + k_i, i = 1, 2, 3, \dots, I, \quad (38)$$

$$\eta_0 = 0, z^j = \eta_{j-1} + h_j, j = 1, 2, 3, \dots, J, \quad (39)$$

where $k_i(\Delta z)$ and $h_j(\Delta \eta)$ are the spacing centering on the point $(z^i, \eta_{j-\frac{1}{2}})$:

$$\begin{aligned} \frac{f_j^i - f_{j-1}^i}{h_j} &= -\frac{H_j^i + H_{j-1}^i}{4} \\ \frac{g_j^i - g_{j-1}^i}{h_j} &= \frac{X_j^i + X_{j-1}^i}{2} \\ \frac{\theta_j^i - \theta_{j-1}^i}{h_j} &= \frac{Y_j^i + Y_{j-1}^i}{2} \\ \frac{\phi_j^i - \phi_{j-1}^i}{h_j} &= \frac{Z_j^i + Z_{j-1}^i}{2} \end{aligned} \tag{40}$$

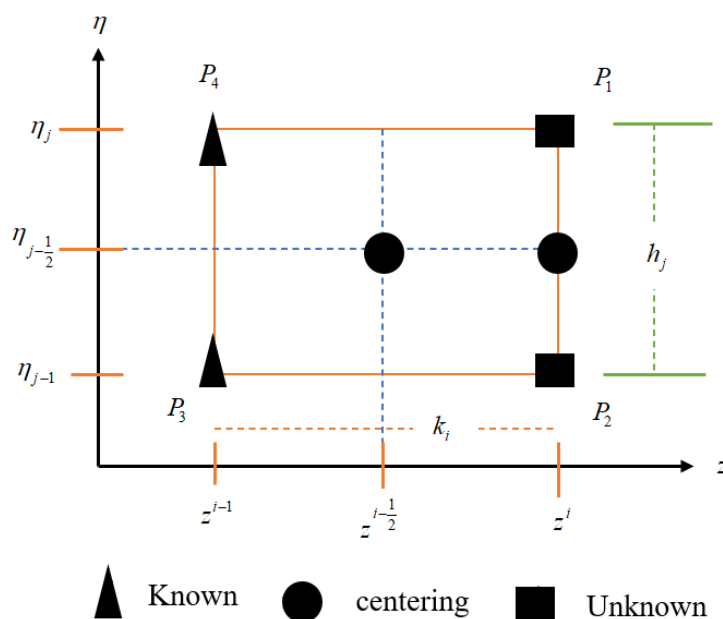


Figure 2. Schematic diagram for domain discretization.

Combining Equation (37) into Equations (31)–(34) and using central difference approximation, we have the following system of equations:

$$L_1 = \left(\frac{H_j^i - H_{j-1}^i}{h_j} \right) - \frac{2B}{A} \left(\begin{aligned} &\left(\frac{H_j^i + H_{j-1}^i}{2} \right)^2 - \left(\frac{f_j^i + f_{j-1}^i}{2} \right)^2 + \left(\frac{g_j^i + g_{j-1}^i}{2} \right)^2 \\ &- S \left[\frac{\eta+1}{4} \left(\frac{H_j^i + H_{j-1}^i}{2} \right) - \left(\frac{f_j^i + f_{j-1}^i}{2} \right) \right] - \lambda \left(\frac{f_j^i + f_{j-1}^i}{2} \right) \end{aligned} \right), \tag{41}$$

$$\frac{X_j^i - X_{j-1}^i}{h_j} - \frac{B}{A} \left(\begin{aligned} &\frac{H_j^i + H_{j-1}^i}{2} \frac{X_j^i + X_{j-1}^i}{2} + 2 \frac{f_j^i + f_{j-1}^i}{2} \frac{g_j^i + g_{j-1}^i}{2} - \\ &S \left[\left(\frac{\eta+1}{2} \right) \frac{X_j^i + X_{j-1}^i}{2} + \frac{g_j^i + g_{j-1}^i}{2} \right] + \lambda \frac{g_j^i + g_{j-1}^i}{2} \end{aligned} \right) = L_2, \tag{42}$$

$$\begin{aligned} &-\frac{\text{Pr}S}{C_1 D} \left[\alpha \frac{\theta_j^i + \theta_{j-1}^i}{2} + \frac{(\eta+1)}{2} \frac{Y_j^i + Y_{j-1}^i}{2} \right] + \frac{A}{BC_1 D} \text{Pr} \frac{H_j^i + H_{j-1}^i}{2} \frac{Y_j^i + Y_{j-1}^i}{2} \\ &-\varepsilon \left(\frac{Y_j^i + Y_{j-1}^i}{2} \right)^2 = \left(1 + \varepsilon \frac{\theta_j^i + \theta_{j-1}^i}{2} \right) \frac{\theta_j^i + \theta_{j-1}^i}{2} L_3, \end{aligned} \tag{43}$$

$$Sc \left[K_c \frac{\phi_j^i + \phi_{j-1}^i}{2} \left(1 - \frac{\phi_j^i + \phi_{j-1}^i}{2} \right)^2 - S(\eta+1) \frac{Z_j^i + Z_{j-1}^i}{2} + \frac{H_j^i + H_{j-1}^i}{2} \frac{Z_j^i + Z_{j-1}^i}{2} \right] = L_4, \tag{44}$$

The boundary constraints are:

$$\begin{aligned} f_0 = 0, g_0 = \omega, H_0 = 0, \theta_0 = 1, Z_0 = K_s \phi_0, \\ f_J \rightarrow 0, g_J \rightarrow 0, \theta_J \rightarrow 0, \phi_J \rightarrow 1, \end{aligned} \quad (45)$$

To linearize the system, we utilized Newton's method for iteration to solve the system of equations above. The block tridiagonal elimination technique was used to solve the system of equations obtained.

4. Results and Discussion

This section addresses the numerous parameters' impact on the associated profiles. The discussion is segmented into subsections.

4.1. Thermal Conductivity and Heat Transfer Rate for Different Nanoparticle Shapes

Figure 3 addresses the variable thermal conductivity of the $CuO, Al_2O_3/C_2H_6O_2$ hybrid nanofluid with different shapes and volume fractions of Al_2O_3 by keeping the volume fraction of CuO $\phi_1 = 0.05$. With $\phi_2 = 0.07$, the blade-shaped nanoparticles would give the best thermal conductivity as compared with the other shapes. Figure 4 delineates the heat transfer analysis by taking different values for the volume fraction of Al_2O_3 and considering various nanoparticle shapes. The results obtained were found to have a good correlation with Figure 2. The blade-shaped Al_2O_3 with $\phi_1 = 0.05, \phi_2 = 0.07$ (the volume fraction of CuO) had a higher heat transfer rate. As the Nusselt number is the fraction of the convective heat transfer and the conductive heat transfer, the blade-shaped particles would have the maximum heat transfer rate. However, the heat transfer rate was minimum for the spherical particles.

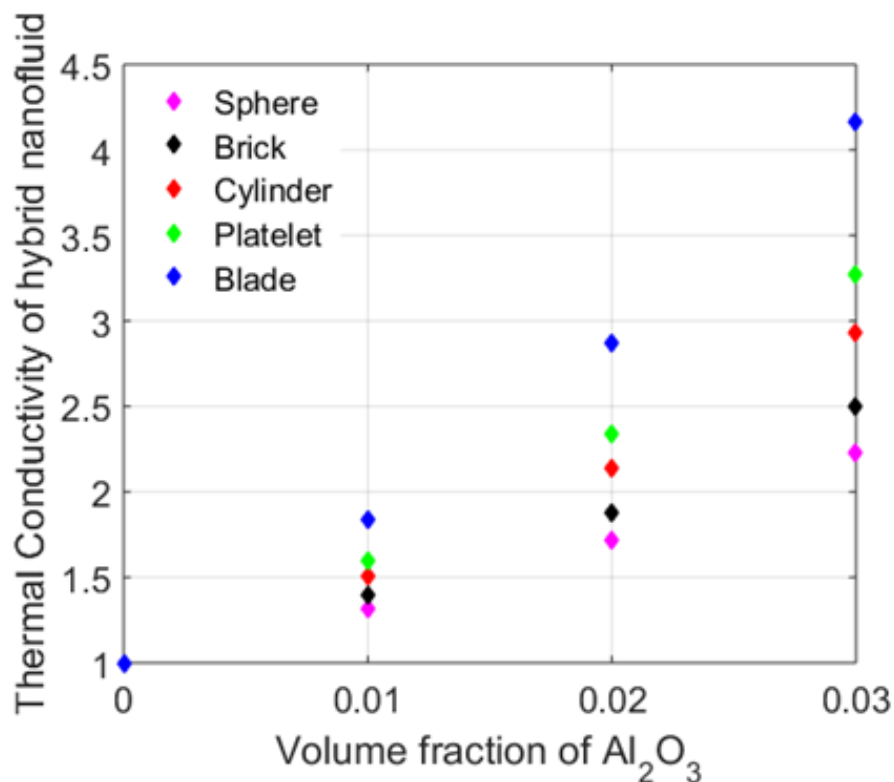


Figure 3. Thermal conductivity of the hybrid nanofluid for various nanoparticle shapes.

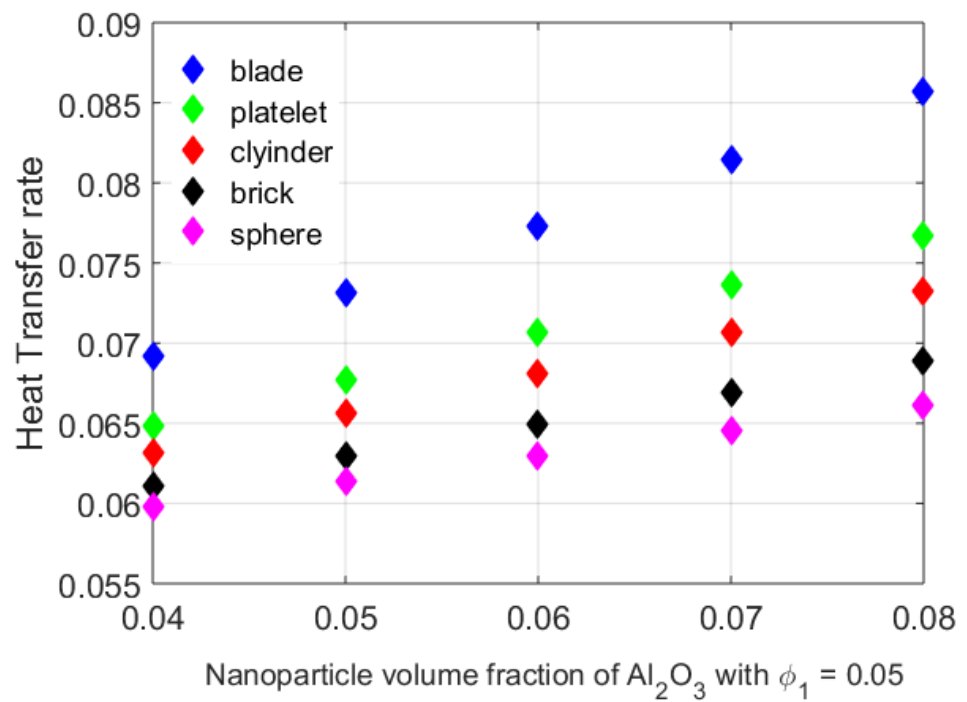


Figure 4. Heat transfer rate for different particle shapes.

4.2. Velocity Profile versus Varying Parameters

Figure 5 gives the radial distribution of velocity for an oscillating disk with varying porosity parameters. The porous media provide a large surface area for the fluid particles to penetrate. As the fluid particles penetrate and are absorbed into the pores, causing a deceleration in the particles' motion. Therefore, the motion of the particles executed by the oscillating disk is inhibited by the presence of porous media. Thus, increasing the value of porosity results in a declining radial profile.

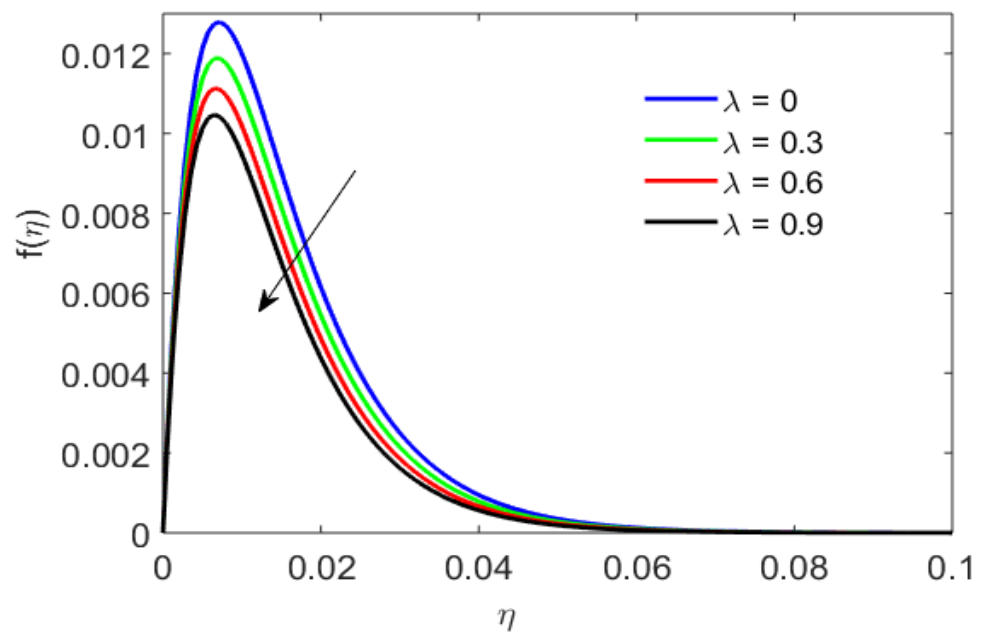


Figure 5. Radial velocity versus porosity parameter.

Figure 6 outlines the axial velocity distribution for varying volume fractions of spherical nanoparticles of Al_2O_3 . With an increase in the concentration of spherical nanoparticles of Al_2O_3 , the axial velocity distribution produces a high curve. Physically, the increase in the volume fraction means that many particles have been added. The momentum transfer process accelerates owing to the enhancement of the axial inflow.

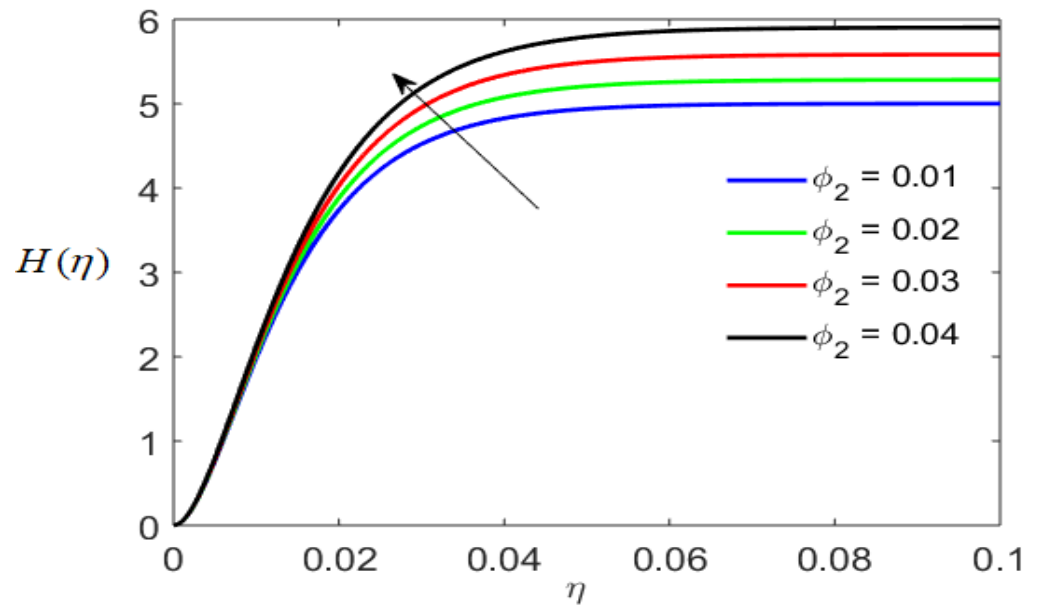


Figure 6. Axial velocity profile for varying volume fractions of nanoparticles of Al_2O_3 .

4.3. Concentration Profile versus Varying Parameters

Figure 7 shows the concentration profile with fluctuations in the surface catalysis and disk parameter. It is noticed that the surface catalysis parameter boosts the reaction rate, causing the concentration profile to decline, while the oscillating disk parameter inhibits the reaction rate at the same rate. Therefore, the concentration profile is increased through contraction and relaxation of the disk.

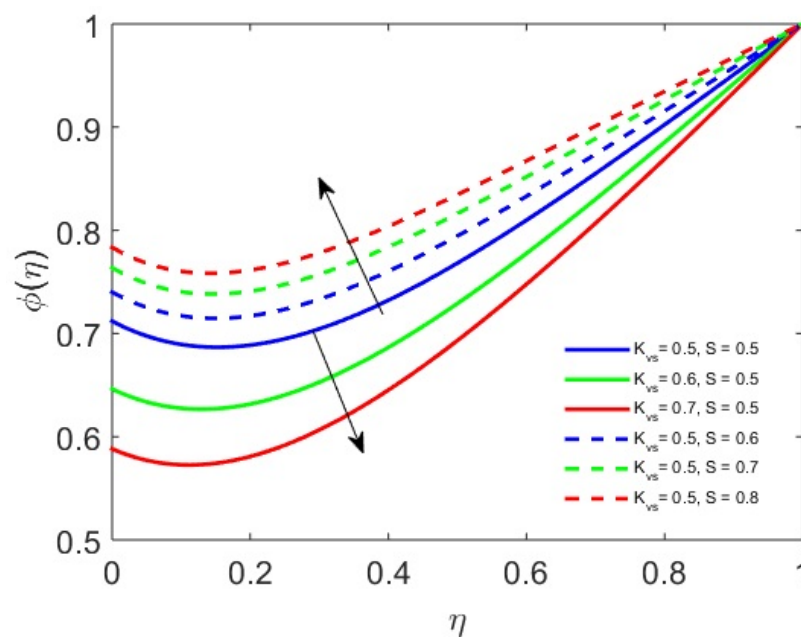


Figure 7. Profile of concentration (ϕ) versus K_{vs} and S .

4.4. Temperature Profile versus Varying Parameters

The temperature profile increases with the expanding and contracting disk parameter S in Figure 8. An escalating thermal profile is observed for increasing values of S . As the fluctuating motion of the disk affects the adjacent layers of the fluid, the energy transmission process increases, causing the thermal profile to increase. Near the disk, the thermal amplitude is at its maximum.

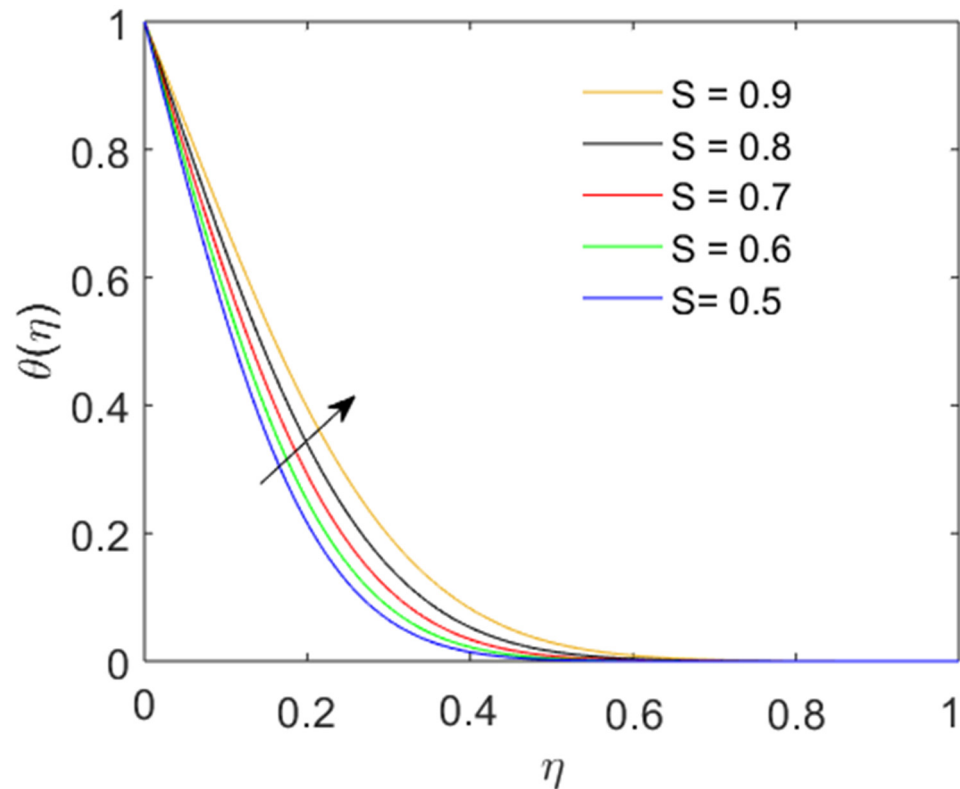


Figure 8. Impact of the disk fluctuation parameter on the thermal profile.

4.5. Numerical Results for Drag Force and the Heat and Mass Transfer Rate

The numerical results for drag force ($\text{Re}^{1/2}C_f$), the heat transfer rate ($\text{Re}^{-1/2}Nu$), and the mass transfer rate ($\text{Re}^{-1/2}Sh$) are delineated by tabulating the results obtained. Table 3 shows the numerical results for the drag force, heat, and mass transfer rate by fixing $K_{vs} = 0.5$, $\lambda = 0.5$, $\Omega = 0.1$, $Sc = 1$, $Pr = 1$, $\alpha = 0.5$, $K_s = 0.5$, $K_c = 0.5$ for increasing values of the oscillating parameter S . This parameter controls the up and down motion of the disk for corresponding positive and negative values of S . With an increasing positive value of S , the drag force near the disk increases. Physically, this points to the reality that the frictional forces increase due to the expansion of the disk. The heat transfer rate is also triggered due to the energy transfer process among the accelerating nanoparticles of the hybrid nanofluid. Similarly, the mass transfer process during the reaction process also accelerates for increasing values of S .

$$\text{Re}^{1/2}C_f = A \left[(f'(0))^2 + (g(0))^2 \right]^{1/2}, \text{Re}^{-1/2}Nu = -C_1 D\theta'(0), \text{Re}^{-1/2}Sh = -\phi'(0). \quad (46)$$

Table 3. Numerical outcomes for drag force and the heat and mass transfer rate with disk fluctuation, keeping [26] $K_{vs} = 0.5, \lambda = 0.5, \Omega = 0.1, Sc = 1, Pr = 1, \alpha = 0.5, K_s = 0.5, K_c = 0.5$.

	$S = 0.1$	$S = 1$	$S = 5$	$S = 10$
$Re^{1/2}C_f$	0.1172760	0.365540	1.90977	3.529200
$Re^{-1/2}Nu$	0.0515513	0.052562	0.0613628	0.078571
$Re^{-1/2}Sh$	0.0000128	0.122310	0.403748	0.450621

Table 4 was constructed to depict the numerical results of the heat transfer rate obtained for various values of the variable wall temperature parameter and the oscillating parameter of the disk. It is seen that for both parameters, the heat transfer rate is enhanced. For a zero value of α , the wall is at a fixed temperature. However, with an increase in α , wall temperature is raised and the heat transfer process increases. The oscillating parameter modifies the impact of the variable wall temperature parameter.

Table 4. Numerical outcomes for the Nusselt number $Re^{-1/2}Nu$ with a varying wall temperature parameter [26] and fixing $K_{vs} = 0.5, \lambda = 0.5, \Omega = 0.5, Sc = 1, Pr = 1, K_s = 0.5, K_c = 0.5$.

	$\alpha = -2$	$\alpha = -1$	$\alpha = 0$	$\alpha = 0.2$	$\alpha = 0.3$
$S = 1$	0.0783255	0.0686171	0.0581365	0.0559352	0.0548204
$S = 5$	0.1552720	0.1243270	0.0855891	0.0764042	0.0715711

Table 5 quantifies the effect of the upward and downward motion of the disk for surface drag force and the heat transfer rate by fixing the disk rotation to $\Omega = 0.5$. For $S < 0$, acceleration of the disk results in a reduction in the drag force. For $S = 0$, the disk is fixed at its position. For $S > 0$, with an increase in S , the decelerating disk slows down the nanoparticles, thus causing the momentum transfer process to increase. Thus, the drag force increases rapidly. The heat transfer rate declines for an accelerating disk ($S < 0$) and increases slowly for a decelerating disk ($S > 0$).

Table 5. Numerical outcomes of drag force and the heat transfer rate under disk fluctuation and keeping [26] $K_{vs} = 0.5, \lambda = 0.5, \Omega = 0.5, Pr = 1, \alpha = 0.3, K_s = 0.5, K_c = 0.5$.

	$S = -0.3$	$S = -0.2$	$S = 0$	$S = 0.5$	$S = 1$	$S = 2$
$Re^{1/2}C_f$	0.4199150	0.357956	1.975870	0.5875330	8.782240	18.17200
$Re^{-1/2}Nu$	0.0327924	0.0245553	0.0213117	0.0530896	0.0548204	0.058571

4.6. Heat Transfer Rate

The heat transfer rate for the hybrid nanofluid is given by:

$$Re^{-1/2}Nu = -C_1 D \theta'(0), \tag{47}$$

where:

$$C_1 = \frac{k_{hnf}}{k_{bf}} = \frac{k_{s_2} - k_{bf}(1-n) + (1-n)\phi_2(k_{bf} - k_{s_2})}{k_{s_2} - (1-n)k_{bf} + \phi_2(k_{bf} - k_{s_2})}, \tag{48}$$

$$D = \frac{k_{bf}}{k_f} = \frac{k_{s_1} - (1-n)k_f + (1-n)\phi_1(k_f - k_{s_1})}{k_{s_1} - (1-n)k_f - \phi_1(k_f - k_{s_1})}, n = \frac{3}{\psi},$$

Table 6 validates the results presented here by comparing them with those of Turkyilmazoglu et al. [26] for various values of S . In this table, we have considered $\phi_1 = 0, \phi_2 = 0$ for the limiting case. For more visibility, the equations are written.

Table 6. Numerical values of $\theta'(0)$ with disk fluctuation, keeping $K_{vs} = 0, \lambda = 0, \Omega = 2, Pr = 1, \alpha = 0.5, K_s = 0, K_c = 0, \phi_1 = 0, \phi_2 = 0$.

	$S = -0.3$	$S = -0.2$	$S = 0$	$S = 0.5$	$S = 1$	$S = 2$
[26]	0.6480310	0.6180880	0.5603780	0.4221660	0.291822	0.052820
Present	0.6480312	0.6180872	0.5603776	0.4221657	0.291821	0.052820

5. Conclusions

The present investigation explored unsteady hybrid nanofluid flow due to a fluctuating spinning disk. Nanoparticles of Al_2O_3 were chosen to detect the best shape for thermal conductivity to obtain an efficient heat transfer process. The physical structure was captured in the form of graphical and tabulated results. The results and discussion section led us to the following significant outcomes.

- Blade-shaped nanoparticles of Al_2O_3 are the best choice for manufacturing the hybrid nanofluid.
- A fluctuating spinning disk inhibits the reaction rate.
- The wall temperature and disk fluctuation parameters increase the heat transfer rate.
- The surface catalysis parameter significantly boosts the reaction rate.
- An increase in the nanoparticle volume fraction boosts the axial velocity profile.

Author Contributions: Conceptualization, M.R.; writing—original draft preparation, S.R.; writing—review and editing, and validation, S.F.A.; software, H.A.S.G. and O.M. All authors have read and agreed to the published version of the manuscript.

Funding: This work was supported by Bahria University, Islamabad.

Informed Consent Statement: Not applicable.

Conflicts of Interest: The authors declare that they have no known competing financial interests or personal relationships that could have appeared to influence the work reported in this study.

Nomenclature

Symbol	Unit	Description	Symbol	Unit	Description
$V = (u, v, w)$	m/s	Components of velocity	λ	Dimensionless	Porosity parameter
Ω	s^{-1}	Angular velocity of the disk	Sc	Dimensionless	Schmidt number
ω	Dimensionless	Constant rotation parameter	A^*, B^*	Dimensionless	Chemical species
S	Dimensionless	Parameter for controlling the up/down motion of the disk	C_a	mol/m ³	Concentration of A^*
$a(t)$	m	Vertical displacement of the disk	C_b	mol/m ³	Concentration of B^*
$\dot{a}(t)$	m/s	Vertical velocity of the disk	k_s, k_c	(mol) ² /s	Reaction rates
p	Pa	Pressure	D_{A^*}, D_{B^*}	m ² /s	Variable diffusion coefficient of chemical species A^*, B^*
ρ_{hnf}	kg/m ³	Density of the hybrid nanofluid	\tilde{S}	m ⁻¹	Interfacial surface area
μ_{hnf}	kgm ⁻¹ s ⁻¹	Dynamic viscosity of the hybrid nanofluid	K_s	Dimensionless	Homogeneous reaction parameter
k^*	m ²	Permeability of the medium	K_{vs}	Dimensionless	Surface catalysis parameter
μ_f	kgm ⁻¹ s ⁻¹	Dynamic viscosity of the fluid	K_c	Dimensionless	Heterogeneous reaction parameter
ρ_f	kg/m ³	Density of the fluid	C_p	Jkg ⁻¹ K ⁻¹	Specific heat
T	K	Temperature	δ	Dimensionless	Ratio of the diffusion coefficient
T_∞	K	Ambient temperature	α	Dimensionless	Wall temperature parameter
T_w	K	Wall temperature	C_∞	mol/m ³	Ambient concentration
Pr	Dimensionless	Prandtl number			
k_{hnf}	J s ⁻¹ m ⁻¹ K ⁻¹	Thermal conductivity of the hybrid nanofluid			
k_{bf}	J s ⁻¹ m ⁻¹ K ⁻¹	Thermal conductivity of the base fluid			
k_f	J s ⁻¹ m ⁻¹ K ⁻¹	Thermal conductivity of the fluid			

Appendix A

The following partial derivatives needed to be utilized in Equations (5)–(11):

$$\frac{\partial u}{\partial t} = \frac{-2rvf}{a^3(t)} - \frac{rvf'}{a^3(t)}\dot{a}(t)(\eta + 1), \frac{\partial u}{\partial r} = \frac{vf}{a^2(t)}, \frac{\partial u}{\partial z} = \frac{rvf'}{a^3(t)}, \frac{\partial p}{\partial r} = 0, \quad (\text{A1})$$

$$\frac{\partial^2 u}{\partial r^2} = 0, \frac{\partial^2 u}{\partial z^2} = \frac{rvf''}{a^4(t)},$$

$$\frac{\partial v}{\partial t} = \frac{-2rvfg}{a^3(t)}\dot{a}(t) - \frac{rvfg'}{a^3(t)}\dot{a}(t)(\eta + 1), \frac{\partial v}{\partial r} = \frac{vg}{a^2(t)}, \frac{\partial v}{\partial z} = \frac{rvfg'}{a^3(t)}, \frac{\partial^2 v}{\partial r^2} = 0, \frac{\partial^2 v}{\partial z^2} = \frac{rvfg''}{a^4(t)}, \quad (\text{A2})$$

$$\frac{\partial w}{\partial t} = -\frac{vH\dot{a}(t)}{a^2(t)} - \frac{vH'}{a^2(t)}\dot{a}(t)(\eta + 1), \frac{\partial w}{\partial r} = 0, \frac{\partial w}{\partial z} = \frac{vH'}{a^2(t)}, \frac{\partial^2 w}{\partial r^2} = 0, \frac{\partial^2 w}{\partial z^2} = \frac{vH''}{a^3(t)}, \quad (\text{A3})$$

$$\frac{\partial T}{\partial t} = -2\alpha c\dot{a}(t)(a(t))^{-2\alpha-1} \left[\alpha\theta + \frac{\eta+1}{2}\theta' \right], \frac{\partial T}{\partial r} = 0, \quad (\text{A4})$$

$$\frac{\partial T}{\partial z} = \frac{c(a(t))^{-2\alpha}}{a(t)}\theta', \frac{\partial^2 T}{\partial r^2} = 0, \frac{\partial^2 T}{\partial z^2} = \frac{c(a(t))^{-2\alpha}}{a^2(t)}\theta'',$$

$$\frac{\partial C_a}{\partial z} = \frac{C_\infty\phi'}{a(t)}, \frac{\partial C_b}{\partial z} = \frac{C_\infty\zeta'}{a(t)}, \frac{\partial C_a}{\partial t} = \frac{C_\infty\phi'\dot{a}(t)(\eta + 1)}{a^2(t)}, \frac{\partial C_b}{\partial t} = \frac{C_\infty\zeta'\dot{a}(t)(\eta + 1)}{a^2(t)}, \quad (\text{A5})$$

On substituting the above partial derivatives, we can obtain the transformed mathematical model.

References

- Choi, S.U.; Eastman, J.A. *Enhancing Thermal Conductivity of Fluids with Nanoparticles*. In *Proceedings of the 1995 ASME International Mechanical Engineering Congress and Exposition, San Francisco, CA, USA, 1995*; ASME, FED 231/MD; Argonne National Lab. (ANL): Argonne, IL, USA, 1995; Volume 66, pp. 99–105.
- Eastman, J.A.; Choi, S.U.S.; Li, S.; Yu, W.; Thompson, L.J. Anomalously increased effective thermal conductivities of ethylene glycol-based nanofluids containing copper nanoparticles. *Appl. Phys. Lett.* **2001**, *78*, 718–720. [[CrossRef](#)]
- Ramzan, M.; Shahmir, N.; Alotaibi, H.; Ghazwani, H.A.S.; Muhammad, T. Thermal performance comparative analysis of nanofluid flows at an oblique stagnation point considering Xue model: A solar application. *J. Comput. Des. Eng.* **2022**, *9*, 201–215. [[CrossRef](#)]
- Shahid, A.; Bhatti, M.M.; Ellahi, R.; Mekheimer, K.S. Numerical experiment to examine activation energy and bi-convection Carreau nanofluid flow on an upper paraboloid porous surface: Application in solar energy. *Sustain. Energy Technol. Assess.* **2022**, *52*, 102029. [[CrossRef](#)]
- Bilal, M.; Ramzan, M.; Mehmood, Y.; Sajid, T.; Shah, S.; Malik, M.Y. A novel approach for EMHD Williamson nanofluid over nonlinear sheet with double stratification and Ohmic dissipation. *Proc. Inst. Mech. Eng. Part E J. Process. Mech. Eng.* **2021**. [[CrossRef](#)]
- Ramzan, M.; Gul, H.; Malik, M.Y.; Ghazwani, H.A.S. Entropy Minimization Analysis of a Partially Ionized Casson Nanofluid Flow over a Bidirectional Stretching Sheet with Surface Catalyzed Reaction. *Arab. J. Sci. Eng.* **2022**, 1–13. [[CrossRef](#)]
- Liu, C.; Akhter, H.; Ramzan, M.; Alaoui, M.K. Impact of melting heat transfer in the bioconvective Casson nanofluid flow past a stretching cylinder with entropy generation minimization analysis. *Int. J. Mod. Phys. B* **2021**, *35*, 2150315. [[CrossRef](#)]
- Ho, C.J.; Cheng, C.Y.; Yang, T.F.; Rashidi, S.; Yan, W.M. Experimental study on cooling performance of nanofluid flow in a horizontal circular tube. *Int. J. Heat Mass Transf.* **2021**, *169*, 120961. [[CrossRef](#)]
- Ramzan, M.; Riasat, S.; Alotaibi, H. EMHD hybrid squeezing nanofluid flow with variable features and irreversibility analysis. *Phys. Scr.* **2022**, *97*, 025705. [[CrossRef](#)]
- Jung, S.Y.; Park, H. Experimental investigation of heat transfer of Al_2O_3 nanofluid in a microchannel heat sink. *Int. J. Heat Mass Transf.* **2021**, *179*, 121729. [[CrossRef](#)]
- Hsiao, K.L. To promote radiation electrical MHD activation energy thermal extrusion manufacturing system efficiency by using Carreau-Nanofluid with parameters control method. *Energy* **2017**, *130*, 486–499. [[CrossRef](#)]
- Hsiao, K.L. Stagnation electrical MHD nanofluid mixed convection with slip boundary on a stretching sheet. *Appl. Therm. Eng.* **2016**, *98*, 850–861. [[CrossRef](#)]
- Suresh, S.; Venkataraj, K.P.; Selvakumar, P.; Chandrasekar, M. A comparison of thermal characteristics of Al_2O_3 /water and CuO /water nanofluids in transition flow through a straight circular duct fitted with helical screw tape inserts. *Exp. Therm. Fluid Sci.* **2012**, *39*, 37–44. [[CrossRef](#)]
- Madhesh, D.; Parameshwaran, R.; Kalaiselvam, S. Experimental investigation on convective heat transfer and rheological characteristics of Cu–TiO₂ hybrid nanofluids. *Exp. Therm. Fluid Sci.* **2014**, *52*, 104–115. [[CrossRef](#)]
- Toghraie, D.; Chaharsoghi, V.A.; Afrand, M. Measurement of thermal conductivity of ZnO–TiO₂/EG hybrid nanofluid. *J. Therm. Anal. Calorim.* **2016**, *125*, 527–535. [[CrossRef](#)]

16. Gul, H.; Ramzan, M.; Nisar, K.S.; Mohamed, R.N.; Ghazwani, H.A.S. Performance-based comparison of Yamada–Ota and Hamilton–Crosser hybrid nanofluid flow models with magnetic dipole impact past a stretched surface. *Sci. Rep.* **2022**, *12*, 29. [[CrossRef](#)]
17. Arif, M.; Kumam, P.; Kumam, W.; Mostafa, Z. Heat transfer analysis of radiator using different shaped nanoparticles water-based ternary hybrid nanofluid with applications: A fractional model. *Case Stud. Therm. Eng.* **2022**, *31*, 101837. [[CrossRef](#)]
18. Bilal, M.; Asghar, I.; Ramzan, M.; Nisar, K.S.; Aty, A.H.A.; Yahia, I.S.; Ghazwani, H.A.S. Dissipated electroosmotic EMHD hybrid nanofluid flow through the micro-channel. *Sci. Rep.* **2022**, *12*, 4771. [[CrossRef](#)]
19. Ramzan, M.; Shahmir, N.; Ghazwani, H.A.S.; Nisar, K.S.; Alharbi, F.M.; Yahia, I.S. Hydrodynamic and heat transfer analysis of dissimilar shaped nanoparticles-based hybrid nanofluids in a rotating frame with convective boundary condition. *Sci. Rep.* **2022**, *12*, 436. [[CrossRef](#)]
20. Zhang, Y.; Shahmir, N.; Ramzan, M.; Ghazwani, H.A.S.; Malik, M.Y. Comparative analysis of Maxwell and Xue models for a hybrid nanofluid film flow on an inclined moving substrate. *Case Stud. Therm. Eng.* **2021**, *28*, 101598. [[CrossRef](#)]
21. Chung, J.D.; Ramzan, M.; Gul, H.; Gul, N.; Kadry, S.; Chu, Y.M. Partially ionized hybrid nanofluid flow with thermal stratification. *J. Mater. Res. Technol.* **2021**, *11*, 1457–1468. [[CrossRef](#)]
22. Gul, H.; Ramzan, M.; Chung, J.D.; Chu, Y.M.; Kadry, S. Multiple slips impact in the MHD hybrid nanofluid flow with Cattaneo–Christov heat flux and autocatalytic chemical reaction. *Sci. Rep.* **2021**, *11*, 14625. [[CrossRef](#)]
23. Shaheen, N.; Ramzan, M.; Alaoui, M.K. Impact of Hall Current on a 3D Casson Nanofluid Flow Past a Rotating Deformable Disk with Variable Characteristics. *Arab. J. Sci. Eng.* **2021**, *46*, 12653–12666. [[CrossRef](#)]
24. Yu, B.; Ramzan, M.; Riasat, S.; Kadry, S.; Chu, Y.M.; Malik, M.Y. Impact of autocatalytic chemical reaction in an Ostwald-de-Waele nanofluid flow past a rotating disk with heterogeneous catalysis. *Sci. Rep.* **2021**, *11*, 15526. [[CrossRef](#)]
25. Riasat, S.; Ramzan, M.; Kadry, S.; Chu, Y.M. Significance of magnetic Reynolds number in a three-dimensional squeezing Darcy–Forchheimer hydromagnetic nanofluid thin-film flow between two rotating disks. *Sci. Rep.* **2020**, *10*, 17208. [[CrossRef](#)]
26. Turkyilmazoglu, M. Fluid flow and heat transfer over a rotating and vertically moving disk. *Phys. Fluids* **2018**, *30*, 063605. [[CrossRef](#)]
27. Von Kármán, T. Über laminare und turbulente Reibung. *Z. Angew. Math. Mech.* **1921**, *1*, 233–252. [[CrossRef](#)]
28. Cochran, W.G. The flow due to a rotating disc. In *Mathematical Proceedings of the Cambridge Philosophical Society*; Cambridge University Press: Cambridge, UK, 1934; Volume 30, pp. 365–375.
29. Liu, C.; Pan, M.; Zheng, L.; Lin, P. Effects of heterogeneous catalysis in porous media on nanofluid-based reactions. *Int. Commun. Heat Mass Transf.* **2020**, *110*, 104434. [[CrossRef](#)]
30. Elattar, S.; Helmi, M.M.; Elkotb, M.A.; El-Shorbagy, M.A.; Abdelrahman, A.; Bilal, M.; Ali, A. Computational assessment of hybrid nanofluid flow with the influence of hall current and chemical reaction over a slender stretching surface. *Alex. Eng. J.* **2022**, *61*, 10319–10331. [[CrossRef](#)]
31. Doh, D.H.; Muthamilselvan, M.; Swathene, B.; Ramya, E. Homogeneous and heterogeneous reactions in a nanofluid flow due to a rotating disk of variable thickness using HAM. *Math. Comput. Simul.* **2020**, *168*, 90–110. [[CrossRef](#)]
32. Hayat, T.; Haider, F.; Muhammad, T.; Ahmad, B. Darcy–Forchheimer flow of carbon nanotubes due to a convectively heated rotating disk with homogeneous–heterogeneous reactions. *J. Therm. Anal. Calorim.* **2019**, *137*, 1939–1949. [[CrossRef](#)]
33. Hussain, Z.; Alshomrani, A.S.; Muhammad, T.; Anwar, M.S. Entropy analysis in mixed convective flow of hybrid nanofluid subject to melting heat and chemical reactions. *Case Stud. Therm. Eng.* **2022**, *34*, 101972. [[CrossRef](#)]
34. Roy, N.C.; Pop, I. Heat and mass transfer of a hybrid nanofluid flow with binary chemical reaction over a permeable shrinking surface. *Chin. J. Phys.* **2022**, *76*, 283–298. [[CrossRef](#)]
35. Ahmed, J.; Khan, M.; Ahmad, L. MHD swirling flow and heat transfer in Maxwell fluid driven by two coaxially rotating disks with variable thermal conductivity. *Chin. J. Phys.* **2019**, *60*, 22–34. [[CrossRef](#)]
36. Abbasi, A.; Al-Khaled, K.; Khan, M.I.; Khan, S.U.; El-Refaey, A.M.; Farooq, W.; Qayyum, S. Optimized analysis and enhanced thermal efficiency of modified hybrid nanofluid (Al_2O_3 , CuO , Cu) with nonlinear thermal radiation and shape features. *Case Stud. Therm. Eng.* **2021**, *28*, 101425. [[CrossRef](#)]
37. Hsiao, K.L. Combined electrical MHD heat transfer thermal extrusion system using Maxwell fluid with radiative and viscous dissipation effects. *Appl. Therm. Eng.* **2017**, *112*, 1281–1288. [[CrossRef](#)]
38. Hsiao, K.L. Micropolar nanofluid flow with MHD and viscous dissipation effects towards a stretching sheet with multimedia feature. *Int. J. Heat Mass Transf.* **2017**, *112*, 983–990. [[CrossRef](#)]